Physica Medica 48 (2018) 84–90

Contents lists available at ScienceDirect

Physica Medica

journal homepage: www.elsevier.com/locate/ejmp

Original paper

# Novel light-guide-PMT geometries to reduce dead edges of a scintillation camera

Beien Wang[a,*], Rob Kreuger[a], Freek J. Beekman[a,b], Marlies C. Goorden[a]

[a] Section of Biomedical Imaging, Faculty of Applied Sciences, Delft University of Technology, Mekelweg 15, 2629 JB Delft, The Netherlands
[b] MILabs B.V., Heidelberglaan 100, 3584 CX Utrecht, The Netherlands

ARTICLE INFO

*Keywords:*
Gamma-ray detectors
Maximum likelihood estimation
Photomultiplier tube
Dead edge

ABSTRACT

Anger cameras based on monolithic NaI scintillators read out by an array of PMTs are predominant in planar gamma imaging and SPECT. However, position estimation of gamma interactions is usually severely degraded near the edges of the scintillator which can be extremely undesirable for applications like breast imaging. Here we propose a relatively cost-effective solution based on the use of scintillators with absorptive edges with an unconventional light-guide-PMT layout employing a maximum likelihood positioning algorithm. The basic design on which we aim to improve consists of a monolithic NaI(Tl) scintillator read out by 3 × 5 square PMTs (conventional layout, CL) that could be suitable for molecular breast imaging. To better detect gamma interactions near the crystal's critical edge, we tried different set-ups: we replaced the 5 large PMTs near the edge by 11 smaller PMTs (small-sensor layout, SSL); we emulated rectangular PMTs along the critical edge by inserting a row of 5 rectangular light-guides that direct the light toward square PMTs placed behind (shifted layout, SL); we inserted rectangular light-guides alternatingly, such that the PMTs are in an interlocking pattern (alternating shifted layout, ASL). The performance of our designs was tested with Monte Carlo simulations. Results showed that SSL, SL, and ASL gave better spatial resolution near the critical edge than CL (3.4, 3.6, and 4.1 mm near the edge compared with 5.3 mm for CL), and thus resulted in a larger usable detector area. To conclude, for applications where small dead edges are crucial, our designs may be cost-effective solutions.

## 1. Introduction

Gamma detectors that deliver information on the interaction position and energy of incoming gamma photons are key elements in nuclear medicine scanners. Both in planar scintigraphy and in SPECT, gamma detectors based on continuous NaI(Tl) scintillators that are read out by an array of photomultiplier tubes (PMTs) – usually referred to as the Anger camera – have been predominant for decades. In Anger cameras, the gamma photon's interaction position and its energy are conventionally estimated using Anger logic [1], which is based on calculating the centroid of the PMT outputs. Anger logic has become popular because it can be simply implemented with a resistor/capacitor network and Anger logic combined with heuristic linearity and non-uniformity corrections provides satisfactory position and energy estimation results in most applications. Unfortunately, the positioning linearity and spatial resolution are usually poor near the scintillator's edges, a situation often referred to as the dead edge effect. This effect has implications for the usable field-of-view of a gamma camera which is smaller than the scintillator's surface.

Although reducing dead edges is almost always profitable to enhance the usable detector surface and thus the system's sensitivity, in whole-body SPECT the presence of dead edges is usually accepted because with the large-area detectors that are commonly applied, the size of the dead edges is relatively small and because not using the detector's edges does not have to lead to image artefacts. However, in other applications, the use of the detector's edges can be absolutely necessary in order to arrive at useful images. Examples of this include planar breast imaging [2,3] and a dedicated multi-pinhole molecular breast tomosynthesis (MP-MBT) technique proposed in our group [4,5]. In the proposed MP-MBT scanner, a woman is lying prone on a patient bed with her breast pendant in a hole in the bed. The breast is mildly compressed and two gamma cameras are placed on either side of the breast close to the chest wall. In simulations, such a design resulted in a tumour-to-background contrast-to-noise ratio 2 – 3 times higher than commercial planar scanners. The edge area of the detector in this design is used to image the part of the breast close to the chest wall. However, in conventional Anger cameras, the dead edge roughly equals the PMT radius and as most common PMTs are two or three inches in diameter,

* Corresponding author.
*E-mail address:* b.wang-1@tudelft.nl (B. Wang).

https://doi.org/10.1016/j.ejmp.2018.04.004
Received 17 February 2018; Accepted 4 April 2018
Available online 10 April 2018

about 25 mm or 40 mm at the edges would be unusable if we would employ a standard Anger camera in MP-MBT. Therefore, a detector with small dead edge is essential for MP-MBT.

To improve positioning linearity near the edges, several solutions have been proposed over the years. In some cases, PMTs were extended over the edges of the scintillator both for continuous crystals [6] and pixelated or semi-pixelated scintillators [7–9]. However, in MP-MBT there is no room for such a placement of PMTs since the scintillator extends till the patient bed. Another option is to read out the continuous crystals with smaller light sensors, including position-sensitive PMTs [10–12], avalanche photodiodes [13,14], silicon photomultipliers [15,16], charge-coupled devices [17], or to use a combination of pixelated scintillators and these small light sensors [18–22]. However, using small light sensors instead of PMTs for large surface gamma detectors (such as in MP-MBT, 240 × 140 $mm^2$ area) leads to enormously increased costs. A third option is to use semiconductor gamma detectors instead of scintillation-based detectors. These detectors transfer gamma energy directly into an electrical signal and are already applied in several dedicated breast scanners [23,24]. Besides being able to reduce dead edges, semiconductor detectors improve energy resolution over scintillator detectors, although several studies have shown that the benefit of this in dedicated breast scanners is limited [25–28]. However, like small light sensors, the use of semiconductor detectors significantly increases the gamma camera's costs over those of the Anger camera.

Besides using new detector materials or advanced light sensors, several algorithms to better decode the scintillation position from the light distribution in PMT-read out scintillators have been proposed, e.g. maximum likelihood estimation [29,30], chi-squared error estimation [31], the *k*-nearest-neighbour method [16], a Gaussian filter algorithm [17], advanced light model fitting [11,14], and different machine learning algorithms [13]. These decoding processes are more sophisticated and also more computationally demanding than weighted averaging, as is done in Anger logic, but they have been proven to be more effective in resolving scintillations near the edges. These algorithms are often used together with black-edge detectors which use absorbing material at the sides of the scintillator [6,7,10,11,29]. Such absorptive edges increase the position dependence of the light spread near the edges, and thus improve position estimation in these areas.

Inspired by several of the above-mentioned elements, the aim of this paper is to propose a novel gamma scintillation detector design that has a cost comparable to that of the Anger camera but has improved spatial resolution and positioning linearity near the edges. This is achieved by using smart light-guide-PMT geometries to emulate smaller light sensors near the edges and by using a black-edge scintillator combined with a maximum likelihood (ML) positioning algorithm. PMTs used have a square shape in order to optimally cover the rectangular scintillator. Different designs are evaluated using Monte Carlo simulations.

## 2. Methods

### 2.1. Gamma detector designs

Detector dimensions are chosen such that they are suitable for the MP-MBT scanner proposed in our group [4,5] which has a minimum requirement for the active detector area of 240 × 140 $mm^2$ and the scintillator thickness is 9.5 mm. We test four different designs in a simulation study which all fulfil the minimum dimension requirement.

The first design (Fig. 1(a)), which is the most basic (therefore dubbed 'conventional layout', CL) comprises a 240 × 180 × 9.5 $mm^3$ NaI(Tl) scintillator, a 14 mm thick glass light-guide, and 15 Hamamatsu R6236 PMTs (60 × 60 $mm^2$ square PMTs with 54 × 54 $mm^2$ photocathodes) [32]. The entrance surface of the scintillator is painted white (reflective) while the edges are black (absorptive). As a comparison, in Section 3.1, we will also show some results for the same design but with a white-edge scintillator. Note that in our design, PMTs placed at the right and left sides of the gamma detector partly extend over the edges. In this way, the left and right edges are effectively read out by half-sized PMTs which is expected to improve resolution and linearity in these edge areas [6]. However, at the upper edge which is assumed to be the critical edge of the detector, such an approach is not feasible as there is no space to allow for this (this is the edge placed close to the patient's chest wall).

An alternative to CL could be the use of smaller PMTs, e.g. Hamamatsu R1548-07 (24 × 24 $mm^2$ square PMTs with (2×) 8 × 18 $mm^2$ photocathodes [32]), which is the second design tested ('small-sensor layout', SSL; Fig. 1(b)). In that case, 21 PMTs would be needed to cover the 240 mm long upper edge. As the price per PMT is approximately constant, the costs for PMTs would increase by 40% while the scintillator size would be reduced to 240 × 144 $mm^2$. In principle, smaller PMT sizes are only required in the direction perpendicular to the edge and one would thus like to use rectangular PMTs if these would be commercially available for the same price. As this is not the case, we propose an alternative design: the 'shifted layout' (SL, Fig. 1(c)). In this layout, an additional light-guide, with a cross-section that is half the PMT area, is inserted in between the original light-guide and each of the upper row PMTs. The additional light-guides are covered by Lambertian reflectors like Polytetrafluoroethylene (PTFE) with 98% reflectivity [33]. The length of the additional light-guide is assumed to be 160 mm, longer than the length of the PMTs (123 mm). The light-guide is assumed to be borosilicate crown glass. A variant on SL is the 'alternating shifted layout' (ASL, Fig. 1(d)), in which the additional light-guides still exist, but the PMTs are placed in an interlocking layout instead of in a conventional grid. Because the second light-guide is half as wide as the PMT front face, the scintillator sizes for SL and ASL are both 240 × 150 $mm^2$. We come back to this reduced area in the discussion section.

### 2.2. Simulations

The performance of our gamma detector designs is assessed by the well-validated Monte Carlo simulation software GEANT4 Application for Tomographic Emission (GATE) [34–36]. The optical surface parameters in GATE are tuned in such a way that the simulator gives the best agreement with our available clinical Anger camera with 3 inch round PMTs. Here we simulate square PMTs, and we assume the light propagation in the new setups remains valid. In Table I. the relevant parameters used in the GATE simulations are listed.

The refractive index of the white reflector was set to 1.0 which reflects the presence of an air gap between the white reflector and the scintillator/light-guide. Furthermore, low reflectivity as reported in [39,40] is assumed which is representative for high-quality black edges because it has been reported that the quality of the black absorber is crucial in the black-edge scintillation camera performance.

To assess spatial resolution and positioning linearity, NEMA suggests to put lead masks with thin parallel slits on the gamma detector and irradiate them with gamma rays from a source placed at a relatively large distance above the detector to approximate parallel rays perpendicularly directed towards the detector surface [41]. In this way, the line response function (LRF) from each slit is obtained, and from these LRFs, positioning linearity and spatial resolution in horizontal and vertical directions are measured. In GATE this measurement is simulated by irradiating the gamma detector with vertical and horizontal line sources of 140 keV gamma photons (energy of $^{99m}$Tc gamma emission). Gamma emitters are evenly distributed in the infinitely thin lines (as is shown in the solid black lines in Fig. 2) and all gamma photons are emitted perpendicular to the detectors. The interval between two neighbouring lines is 10 mm, and the outer horizontal and vertical lines are all 2 mm from the edges of the scintillator.

To obtain the light collection map and linearity correction map for Anger logic estimation (further discussed in Sections 2.3 and 2.4), the gamma detectors are also irradiated by point sources of 140 keV gamma photons, and the point response functions are determined. From each

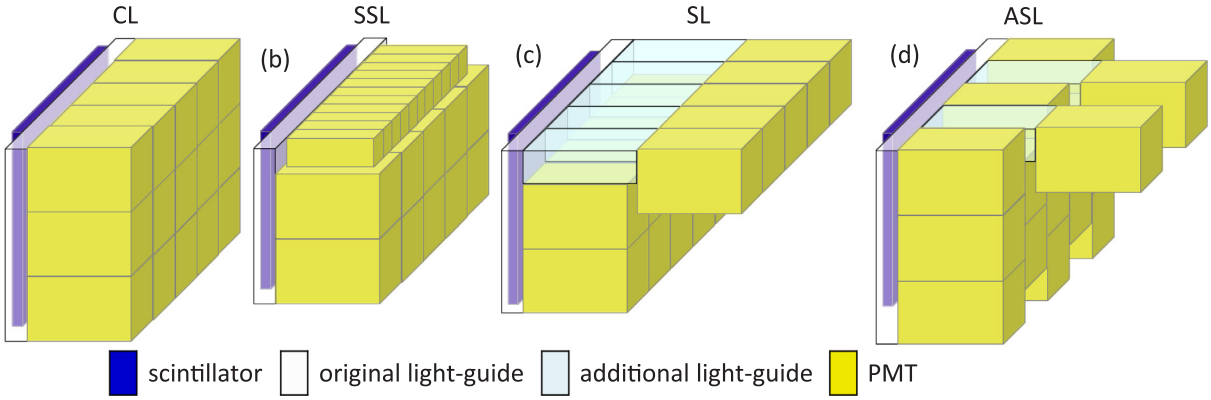


**Fig. 1.** The four gamma detector designs tested in this paper. The scintillator, light-guide and PMTs are shown schematically for (a) CL, (b) SSL, (c) SL and (d) ASL.

**Table 1**
Settings in simulation.

| Parameter in GATE | Status |
|---|---|
| Photoelectric effect | StandardModel |
| Compton scatter | StandardModel |
| Optical simulation | Scintillation, OpticalAbsorption, OpticalRayleigh, OpticalBoundary |
| Photocathode | Efficiency: 0.29 [32] |
| Black absorber | Reflectivity: 0.05, refractive index: 1.8 |
| White reflector | Lambertian reflection, reflectivity: 0.98, refractive index: 1.0 |
| Interface (scintillator to light-guide) | Roughened |
| Scintillator (NaI(Tl)) | Density: 3.67 g/cm$^3$, light yield: 38,000 photons/MeV, intrinsic energy resolution: 5% [37,38], refraction index:1.85 |
| Light-guide (glass) | Density: 2.50 g/cm$^3$, refraction index: 1.50, absorption length: 3.11 m |

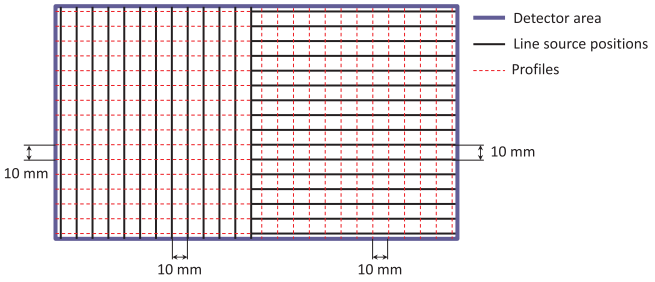


**Fig. 2.** Line sources irradiate the gamma detector. The left part of the detector is irradiated by vertical line sources (marked by solid black lines) while the right part of the detector is irradiated by horizontal line sources. The profiles of the LRFs are taken at every intersection of the solid black lines with dashed red lines. (For interpretation of the references to colour in this figure legend, the reader is referred to the web version of this article.)

point source, about 2000 gamma photons are emitted perpendicular to the gamma detector's surface. These gamma point sources are placed in a grid of 5 mm interval over the whole detector.

To apply ML estimation, a series of reference PMT outputs, i.e. the expected number of optical photons detected by each PMT for all possible scintillation locations, should be obtained. These reference PMT outputs are extracted from the PRF simulation. The light collection spectrum of each point source is obtained and the interactions in the ± 10% window around 140 keV are averaged and then taken as reference PMT outputs. In this case, the reference PMT outputs also include scatter in the photopeak. Then reference PMT outputs are obtained at a 1 mm grid by cubic interpolation of the 5 mm-interval reference PMT outputs and used for ML estimation.

### 2.3. Data processing

We use GATE simulation results to generate a list of gamma photon detections, in which the number of optical photons sensed by each PMT (the PMT output) in every interaction is recorded. These data are then contaminated by simulated readout noise which is Gaussian distributed with zero mean and a full-width at half-maximum (FWHM) of 6 photons. This noise level is estimated based on the measurement from readout electronics in our lab. We use this list of data as the input to Anger and ML position estimation. Anger logic is implemented as an output-weighted average of PMT coordinates. To improve Anger estimation resolution, a threshold is applied to each PMT output. Only the PMTs with outputs above the threshold are used in the weighted average process. The threshold in our case is set as 3% of the total summed PMT output at every detection. We apply a linearity correction as is commonly done for Anger cameras in the same way as described in [42] with linearity correction map obtained from the PRF data.

The ML positioning algorithm is based on the assumption that if the gamma photon's energy and the interaction position are fixed, the number of scintillated optical photons detected on each PMT ($\boldsymbol{n} = [n_1 n_2 \cdots n_M]$, $M$ PMTs in total) is Poisson distributed [29]. Of course the readout noise is not Poisson-distributed, but as its FWHM of 6 photons is less than 5% of the mean PMT output, using a Poisson distribution is a tolerable approximation in this case. If the Poisson mean of the output of PMT $m$ ($\bar{n}_m(x,y)$) for a gamma photon of a certain energy is known for every possible gamma interaction location, one can write the probability that an interaction occurring at location $(x,y)$ resulted in output $\boldsymbol{n}$ as:

$$\mathrm{pr}(\boldsymbol{n}\,|x,y) = \prod_{m=0}^{M} \frac{[\bar{n}_m(x,y)]^{n_m}}{n_m!} e^{-\bar{n}_m(x,y)}. \tag{1}$$

Note that in this equation we do not take the dependence of the PMT outputs on the depth of interaction in the crystals into account, rather $\bar{\boldsymbol{n}}_m$represents an average over different depths. In this work, the mean outputs $\bar{n}_m(x,y)$ were obtained by interpolating simulated PRFs, as is described in Section 2.2. The most likely gamma photon interaction location $(\hat{x},\hat{y})$is the one that maximizes (1):

$$(\hat{x},\hat{y}) = \arg\max_{x,y} \mathrm{pr}(\boldsymbol{n}|x,y) \tag{2}$$

In practice, the logarithm of $(\boldsymbol{n}|x,y)$ is maximized which simplifies the calculation and gives exactly the same result.

The searching strategy used in this paper to obtain the most likely interaction position is a contracting-grid algorithm based on the one described in [43]. This method can quickly search for the target in a multi-dimensional space by dividing the search into grids of different intervals, and as long as $\bar{n}_m(x,y)$is a smoothly changing function of location, it should give the same result as an exhaustive search. The initial search is done on a coarse grid such that the target's rough location is

obtained. Later on, with the found rough location as the starting point, this search is repeated on an ever finer grid. Though the search is exhaustive in every grid, the total time complexity is much less than exhaustively searching the whole range in the fine grid. The grids used here are

1. 5-by-5 grid with 13 mm interval;
2. 5-by-5 grid with 5 mm interval;
3. 3-by-3 grid with 3 mm interval;
4. 3-by-3 grid with 2 mm interval;
5. 3-by-3 grid with 1 mm interval.

So in total 77 iterations are required for every detected interaction and the searching range is $52 \times 52\ mm^2$. The starting point is the Anger estimated position. The resulting images will have a pixel size of 1 mm.

### 2.4. Performance evaluation

In order to evaluate the gamma camera's performance, we use the LRFs to determine positioning linearity and spatial resolution, and PRFs to obtain the total light collection and the energy resolution. To note, the energy resolution here is not calculated from the energy spectrum but from the light collection spectrum: a histogram of the total number of photons collected (sum of all PMT outputs) for each interaction.

Spatial resolution in this paper is obtained by fitting a Gaussian function to the LRFs and then determining its FWHM. To obtain information on how spatial resolution varies over the detector, profiles (one pixel-width; 1 mm) of the LRFs are taken along all dashed red lines in Fig. 2 which have 10 mm spacing. For visualization purposes, we then interpolate the spatial resolution distribution on the whole detector to 1 mm intervals. Spatial resolution in horizontal and vertical directions ($R_{ix}$ and $R_{iy}$) is presented separately, and we also calculate an "averaged" spatial resolution by determining the root-mean-square (RMS) in both directions: $R_{ixy} = \sqrt{(R_{ix}^2 + R_{iy}^2)/2}$ Energy resolution ($R_{iE}$) is defined to be the FWHM of a Gaussian fit to the light collection spectrum divided by the mean of the fit (given as a percentage) at each point source position.

As postulated by NEMA [41], positioning linearity of the detectors is given by differential linearity which is defined as the standard deviation of every estimated LRF in the direction perpendicular to the lines. Finally, we also provide the usable field-of-view (UFOV) of the different designs which we define as the area where $R_{ixy} < 5$ mm.

## 3. Results

### 3.1. Black-edge gamma detector and ML algorithm

In Fig. 3, the LRFs obtained with the CL are shown for a white-edge scintillator read out by Anger logic (a) and by the ML algorithm (b), and for a black-edge scintillator employing the ML algorithm (c). LRFs are only shown on half the detector surface because of the horizontal symmetry of the layout. It is clear that if a scintillator with white reflecting edges is used, a significant part near the scintillator's edges is not usable (about 30 mm from the upper and lower edges, and 15 mm from the left and right edges), even if ML estimation is used. With Anger estimation (Fig. 3(a)), the lines near the edge pile up inwards to about half a PMT-size from the edge, while with ML estimation (b), the lines up to a distance of half the PMT size from the edge are severely blurred and cannot be distinguished anymore. For the black-edge detector with ML estimation (Fig. 3(c)), the position estimation at the edge is much improved compared to (a) and (b), though at the corners resolution is clearly reduced. Anger estimation on a black-edge detector is not an option because a weighted average algorithm would give even poorer positioning linearity with the lower number of sensed optical photons on the near-edge PMTs [44].

For the same conventional detector layout, Fig. 4 shows three example light collection spectra obtained for the white-edge detector (a) and black-edge detector (b) at three example locations (centre, edge, and corner). Clearly, the total number of optical photons collected depends on where in the scintillator the gamma interaction took place; more optical photons are collected for events in the centre compared to events near the scintillator's edge (5 mm to one edge in this example) and corner (5 mm to two edges). This effect of varying light collection over the scintillator is much stronger when black absorptive edges are used; in that case edge scintillations have almost 50% less light collection than in the centre while in the corners the light collection is reduced by about 65%. For the white-edge detector, the largest light loss is about 30% at the corner of the detector, but as the edges and corners of white-edge detectors cannot be used and the light collection at edges of the usable area is the same as in the centre, in practice a global light collection window is usually set for subsequent scatter rejection [45]. From the spectra, one can conclude that a global light collection window is not applicable in black-edge scintillation detectors.

### 3.2. Different detector layouts

In Fig. 5, simulation results for all PMT layouts are compared. All of the four detectors have black edges and positioning is thus done with ML estimation. For the same reason as in Fig. 3, LRFs on only half of the detector area are shown. From the LRFs in Fig. 5(e) – (h), spatial resolution maps in horizontal (i) – (l) and vertical (m) – (p) directions are calculated. The light collection maps shown in Fig. 5(q) – (t) are obtained from the PRFs. It can be seen that the four layouts have similar resolution in horizontal direction (about 3.6 mm on average), but that SSL, SL, and ASL show better resolution in vertical direction close to the upper critical edge (3.4 mm, 3.6 mm, and 4.1 mm up to 30 mm to the critical edge compared to 5.3 mm in CL). For SSL and SL, the places with poor resolution are all near the lower edge, while for ASL, they are more spread over the detector area. For all four detector designs, light collection at the centre of the detector is higher than that at the edge.

In Table 2, the mean spatial resolutions in horizontal and vertical

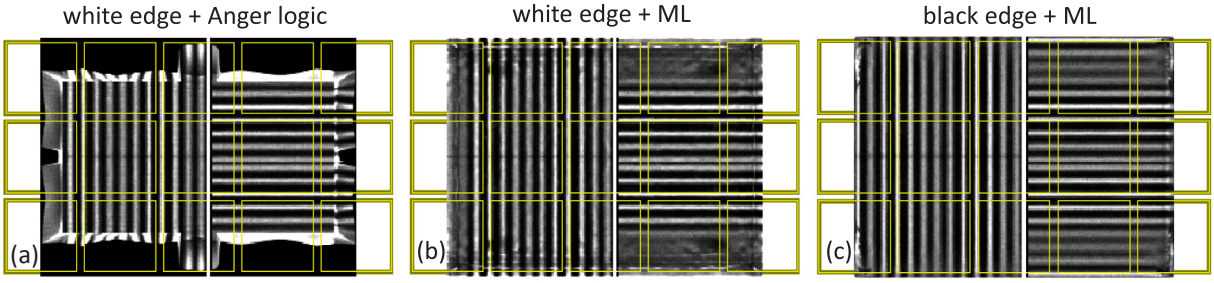


**Fig. 3.** The LRFs of the CL with different edge treatment and positioning algorithm combinations. The yellow squares in the figures mark the effective area of the PMTs. The critical camera edge is the upper edge. (For interpretation of the references to colour in this figure legend, the reader is referred to the web version of this article.)

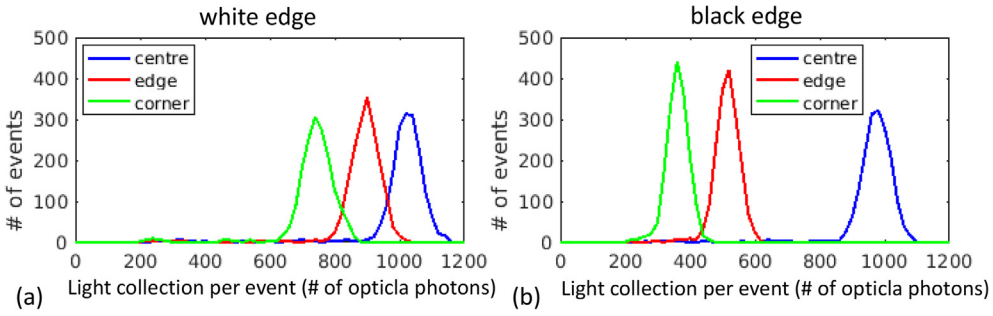


**Fig. 4.** Example light collection spectra for CL with scintillators with (a) white edge and (b) black edge treatments. Three typical positions are tested: centre, edge (5 mm to one edge of the scintillator), and corner (5 mm to two edges of the scintillator). These spectra were obtained by simulating an irradiation with 2000 gamma photons per position.

directions ($R_{ix}$ and $R_{iy}$) over the whole detector obtained from Fig. 5(i) – (p) are listed. The differential linearity (lin.) in horizontal and vertical directions is calculated from the LRFs 4 (e) – (h). The UFOVs are determined by $R_{ixy} < 5$ mm. The centre, edge (< 8 mm from an edge), and corner (< 8 mm from two edges) mean energy resolutions ($R_{iE}$) are calculated (see Section 2.3).

## 4. Discussion

From Fig. 3 it is clear that the use of black absorptive edges and ML estimation can largely improve positioning linearity near the edges compared with a traditional white-edge detector with Anger logic positioning, though the spatial resolution near the edges is still rather poor. For all four layouts in Fig. 5(e) – (h), significant distortion in LRFs is not observed except in the corners. The distorted area in the three non-conventional layouts is smaller than that in the CL, which is also reflected by the spatial resolution-defined UFOV in Table 2. In the simulation study of MP-MBT [5] we assumed that the dead edge of the detector was 5 mm, and SSL, SL, and ASL seem to be able to achieve this goal as the LRFs nearest (2 mm) to the scintillator edges are resolved.

**Table 2**
Spatial resolution, positioning linearity, UFOV, and energy resolution obtained for different layouts.

| | $R_{ix}$ (mm) | $R_{iy}$ (mm) | lin. x (mm) | lin. y (mm) | UFOV (%) | $R_{iE}$ centre (%) | $R_{iE}$ edge (%) | $R_{iE}$ corner (%) |
|---|---|---|---|---|---|---|---|---|
| CL | 3.54 | 4.31 | 0.10 | 0.27 | 81.5 | 11.6 | 14.4 | 16.4 |
| SSL | 3.58 | 4.28 | 0.11 | 0.21 | 86.4 | 12.1 | 15.4 | 17.6 |
| SL | 3.70 | 4.19 | 0.11 | 0.18 | 84.1 | 12.1 | 15.1 | 16.8 |
| ASL | 3.67 | 3.85 | 0.12 | 0.17 | 90.0 | 11.9 | 14.7 | 16.1 |

Note that the SSL, SL and ASL result in shorter detectors than the CL, as we keep the same number of rows of PMTs and the MP-MBT application only requires a 140 mm long detector. If one would like to compare different designs at equal detector area, one has to add an extra row of PMTs to the non-conventional designs resulting in a larger part of the scintillator being covered. Adding another row of PMTs would require five more PMTs for SL or SSL, and two more PMTs for ASL. The performance of such extended detectors can be predicted through vertical

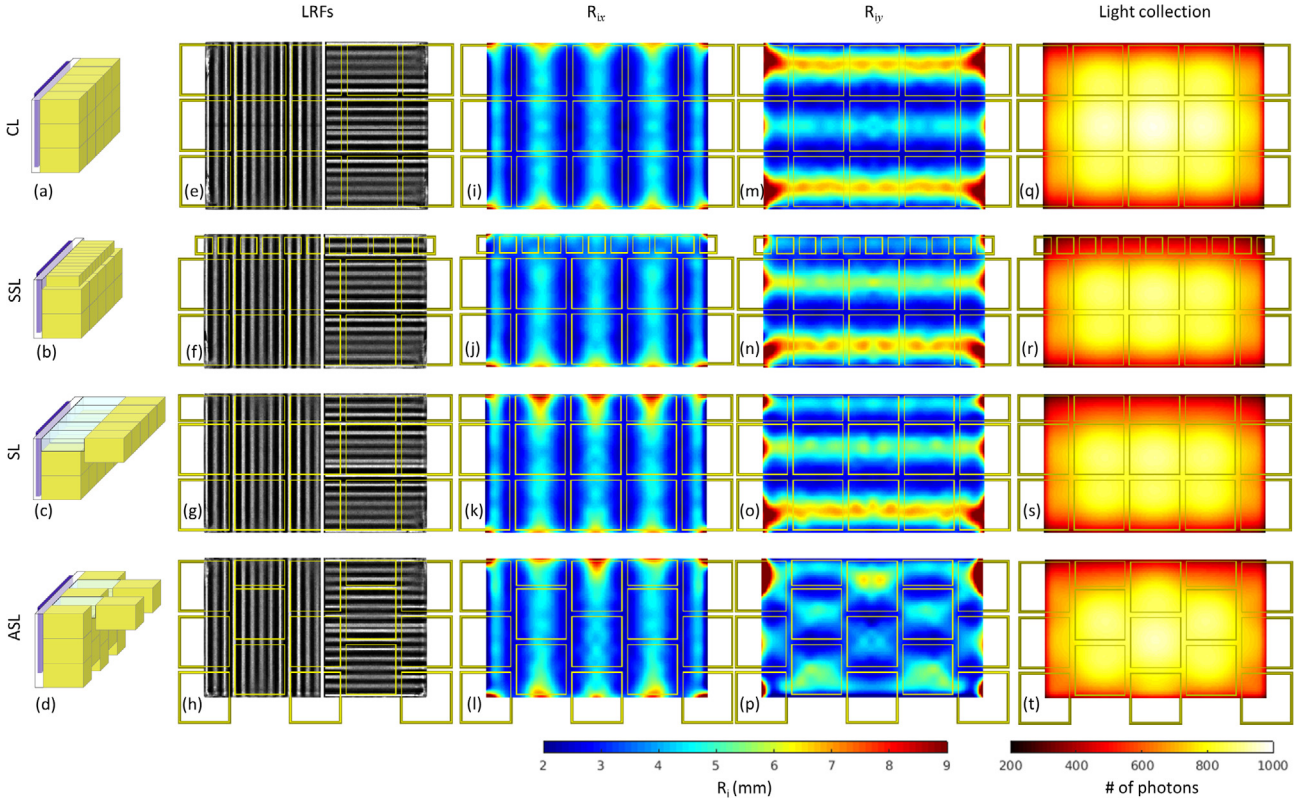


**Fig. 5.** The LRFs, spatial resolution in horizontal and vertical directions ($R_{ix}$ and $R_{iy}$), and light collection of the four gamma detector layouts. The yellow rectangles in the graphs mark the effective area of the PMTs. The energy resolution maps are not shown but the representative values are provided in Table 2. All four layouts are black-edge detectors using ML estimation. (For interpretation of the references to colour in this figure legend, the reader is referred to the web version of this article.)

**Table 3**
Usable area per PMT of different designs.

| | # of PMTs | UFOV (%) | UFOV (%)/PMT | Actual usable area ($mm^2$)/PMT |
|---|---|---|---|---|
| CL | 15 | 81.5 | 5.4 | 2347 |
| SSL | 21 | 86.4 | 4.1 | 1422 |
| SL | 15 | 84.1 | 5.6 | 2018 |
| ASL | 15 | 90.0 | 6.0 | 2160 |
| Extended SL* | 20 | 91.2 | 4.6 | 1970 |
| Extended ASL* | 17 | 89.7 | 5.3 | 2279 |

* The extended ($240 \times 180\,mm^2$ size) detector performance is estimated from vertical symmetry instead of an extra Monte Carlo simulation.

symmetry: PMT layouts in the UFOV of (180 mm long) extended detectors are vertically symmetric, thus we can simply mirror the upper 90 mm of the resolution map down to roughly predict the resolution in the lower 90 mm. This is still an estimation as the lower edge should have better resolution than suggested by simply mirroring as no additional light-guide would be needed there. For extended SL, the vertical and horizontal resolutions are 3.84 mm and 3.76 mm, and for extended ASL, they are 4.05 mm and 3.66 mm. For SSL, such symmetry does not exist, so the performance cannot be predicted. Table 3. estimates the usable area per PMT of different layouts including the two extended layouts ($240 \times 180\,mm^2$).

Although the CL detector surface is larger than the other three simulated layouts, the actual usable area is not always much different (see Table 3): the actual usable area (the number of PMTs multiplied by the actual usable area per PMT) in SSL ($21 \times 1422\,mm^2$) is 85% of CL ($15 \times 2347\,mm^2$); SL's usable area ($15 \times 2018\,mm^2$) is also 86% of that of CL; ASL ($15 \times 2160\,mm^2$) has a usable area that is 92% of that of CL. From the quotations we got, the cost of an additional light-guide, and the extra cost of the 160 mm longer detector box would make the whole gamma detector (scintillator + PMTs + readout electronics + detector box) price increase by less than 4% when ASL is constructed compared to CL. Other solutions, e.g. applying small light sensor, scintillator pixilation, and using semiconductor detectors are usually much more expensive. For example, according to the online price of SiPMs [46], using SiPMs to cover a detector surface as large as ours will be 5 times as expensive as using PMTs, resulting in a doubling of the total detector price. This estimate does not even include the costs for extra electronic read-out channels.

From the spatial resolution maps in Fig. 5(i) – (p), it is clear that the spatial resolution is always best in the interstices of PMTs, while it is the poorest in the centres of PMTs, especially in the centres of PMTs near edges. Such a phenomenon is also observed in other detectors using ML estimation or Anger logic [29,31] and it is not difficult to understand: in scintillator detectors, position estimation accuracy depends on the sensitivity of the light distribution (PMT outputs in this case) to the exact interaction position and the total amount of light collection. In the centres of PMTs, light spread is not that sensitive to the scintillation position, while in the interstices, a subtle position change already leads to large light spread changes, i.e. PMT output changes; in the centres of the near-edge PMTs, PMT outputs are the least location-sensitive and the total photon collection is smaller than in the centre of the detector; therefore, the spatial resolution is worst in these places. The purpose of designing ASL is to reduce the number of large PMTs at the edges and avoid continuous low-resolution regions, e.g. PMTs at lower rows in SSL and SL (Fig. 5(n) and (o)). Note that the light collection above the centres of the PMTs is higher than in the interstices. We believe that a trade-off between light collection and the sensitivity of PMT outputs to the exact interaction position may result in the minor fluctuations in the top row of the spatial resolution map for ASL (e.g. there appear to be two poor resolution centres close to the PMTs' centre).

An issue with the proposed designs may be the light collection loss due to the black edges. In Fig. 5(q) – (t) a reduced light collection near the edges is clearly observed, as well as in Fig. 4 in which the difference between black- and white-edge detectors is obvious. For the three unconventional designs (Table 2), the energy resolution in the central region of the detectors is always poorer than for the CL. This is because the centre-to-edge ratio in the CL is the highest, so that the black edges absorb less scintillated light from the central part of the detector. As a result of black edges, a global energy window over the whole detector, as is in most Anger cameras, is not suitable. Instead, a scintillation-position-dependent energy window could be applied, as long as the PMT outputs are sufficiently distinct in different interaction positions for different amounts of energy deposition. An efficient way for energy windowing might be to apply a rough (localised) energy window based on the Anger estimated scintillation location.

Furthermore, in the simulation, the attenuation of optical photons in light-guides is assumed to be the attenuation of borosilicate crown glass [47]. For the additional light-guides inserted in front of the upper row of PMTs, the attenuation of the 160 mm glass, the absorption in the PTFE reflector, and the absorption at the transitions of different materials result in about 20% less light collection on the PMTs attached compared to directly mounting PMTs to the 14 mm-thick light-guide. This light loss leads to poorer energy resolution at the upper edge (see Fig. 5(s)). Additionally, poorer photon statistics degrades the spatial resolution in SL and ASL, as is specially obvious in the middle of the second row of PMTs. Such a deterioration of spatial resolution compared to CL is also observed in SSL, which we believe is probably because of the of lower fill-factor of smaller PMTs (0.5 instead of 0.8 for the R6236 PMTs).

In the current study both the calibration and the line source test are based on the same Monte Carlo simulations, which is an 'ideal' situation while in practice the exact response of scintillator, light-guide and PMTs may be unknown. We have tried to keep experimental practicality into mind. For example, the simulated processes of obtaining the PRFs and LRFs are not impractical, as they are based on NEMA recommendations for actual measurements, as is mentioned in Section 2.2. Also some realistic non-ideality is created as we interpolate calibration PRFs simulated on a 5 mm grid to a smaller 1 mm grid. However, in practice there may be some scatter in the mask for calibration and the collimated gamma beams are wider than in the simulations where we assumed infinitely small points sources, e.g. a width of about 1 mm is common. As the FWHM of PRFs is mostly 2–4 mm, we expect that this effect is not too large. Also, the mechanical and electrical stability of the system is not included in the simulations. However, from our experience with Anger cameras ($470 \times 590\,mm^2$ NaI scintillator readout by 3 inch PMTs), the mechanical parts can be produced rather reliable (0.01 mm motion error), and the electronics (especially PMTs) perform consistently for years after the first few days run-in period. The breast detector should not be more fragile than other existing systems.

## 5. Conclusion

The black-edge ASL gamma detector using ML estimation proposed in this paper can be a cost-effective solution for better resolving the dead edges. SSL and SL give better spatial resolution near the critical edge, but the resolution in other parts of the detector is compromised. As a drawback of using black edges, the light collection over the detector will be non-uniform, which requires extra work to apply a position-dependent energy window. Experimental tests have to be done to assess the real performance of the new design and confirm the results of this paper.

## Declarations of interest

None.

## Acknowledgement

Funding: This work is supported by the Dutch Organization for Scientific Research (NWO) under the VIDI grant [Grand number 12371] Focused imaging of tumors.

## References

[1] Anger HO. Scintillation camera. Rev Sci Instrum 1958;29:27–33.
[2] Hruska CB, O'Connor MK. Nuclear imaging of the breast: translating achievements in instrumentation into clinical use. Med Phys 2013;40.
[3] Fowler AM. A molecular approach to breast imaging. J Nucl Med 2014;55:177–80.
[4] Beekman FJ. Gamma radiation imaging apparatus. 2011. US20110158384.
[5] van Roosmalen J, Goorden MC, Beekman FJ. Molecular breast tomosynthesis with scanning focus multi-pinhole cameras. Phys Med Biol 2016;61:5508.
[6] Freifelder R, Haigh AT, Karp JS. Reducing edge effects and improving position resolution in position-sensitive NaI(Tl) detectors. IEEE Trans Nucl Sci 1993;40:208–13.
[7] Rozler M, Liang HN, Chang W. Development of a cost-effective modular pixelated NaI(Tl) detector for clinical SPECT applications. IEEE Trans Nucl Sci 2012;59:1831–40.
[8] Wong WH, Uribe J, Hicks K, Hu GJ. An analog decoding BGO block detector using circular photomultipliers. IEEE Trans Nucl Sci 1995;42:1095–101.
[9] Surti S, Freifelder R, Karp JS. Slotted surface treatment of position-sensitive NaI(Tl) detectors to improve detector performance. IEEE Trans Nucl Sci 2001;48:2418–23.
[10] Deprez K, Vandenberghe S, Vandeghinste B, Van Holen R. FlexiSPECT: A SPECT system consisting of a compact high-resolution scintillation detector (SPECTatress) and a lofthole collimator. IEEE Trans Nucl Sci 2013;60:53–64.
[11] Domingo-Pardo C, Goel N, Engert T, Gerl J, Isaka M, Kojouharov I, et al. A position sensitive gamma-ray scintillator detector with enhanced spatial resolution, linearity, and field of VIEW. IEEE Trans Med Imaging 2009;28:2007–14.
[12] Joung J, Miyaoka RS, Lewellen TK. CMiCE: a high resolution animal PET using continuous LSO with a statistics based positioning scheme. Nucl Instrum Meth A 2002;489:584–98.
[13] Bruyndonckx P, Lemaitre C, van der Laan DJ, Maas M, Schaart D, Wang YG, et al. Evaluation of machine learning algorithms for localization of photons in undivided scintillator blocks for PET detectors. IEEE Trans Nucl Sci 2008;55:918–24.
[14] Li Z, Wedrowski M, Bruyndonckx P, Vandersteen G. Nonlinear least-squares modeling of 3D interaction position in a monolithic scintillator block. Phys Med Biol 2010;55:6515–32.
[15] Marcinkowski R, Mollet P, Van Holen R, Vandenberghe S. Sub-millimetre DOI detector based on monolithic LYSO and digital SiPM for a dedicated small-animal PET system. Phys Med Biol 2016;61:2196–212.
[16] Schaart DR, van Dam HT, Seifert S, Vinke R, Dendooven P, Lohner H, et al. A novel, SiPM-array-based, monolithic scintillator detector for PET. Phys Med Biol 2009;54:3501–12.
[17] Korevaar MAN, Heemskerk JWT, Goorden MC, Beekman FJ. Multi-scale algorithm for improved scintillation detection in a CCD-based gamma camera. Phys Med Biol 2009;54:831–42.
[18] Krizsan AK, Lajtos I, Dahlbom M, Daver F, Emri M, Kis SA, et al. A promising future: comparable imaging capability of MRI-compatible silicon photomultiplier and conventional photosensor preclinical PET systems. J Nucl Med 2015;56:1948–53.
[19] Miller BW, Barber HB, Barrett HH, Shestakova I, Singh B, Nagarkar VV. Single-photon spatial and energy resolution enhancement of a columnar CsI(Tl)/EMCCD gamma-camera using maximum-likelihood estimation. Proc SPIE. 2006;6142.
[20] Gruber GJ, Choong WS, Moses WW, Derenzo SE, Holland SE, Pedrali-Noy M, et al. A compact 64-pixel CsI(Tl)/Si PIN photodiode imaging module with IC readout. IEEE Trans Nucl Sci 2002;49:147–52.
[21] Raylman RR, Majewski S, Kross B, Popov V, Proffitt J, Smith MF, et al. Development of a dedicated positron emission tomography system for the detection and biopsy of breast cancer. Nucl Instrum Meth A 2006;569:291–5.
[22] Doshi NK, Shao YP, Silverman RW, Cherry SR. Design and evaluation of an LSO PET detector for breast cancer imaging. Med Phys 2000;27:1535–43.
[23] Mueller B, O'Connor MK, Blevis I, Rhodes DJ, Smith R, Collins DA, et al. Evaluation of a small cadmium zinc telluride detector for scintimammography. J Nucl Med 2003;44:602–9.
[24] Butler JF, Lingren CL, Friesenhahn SJ, Doty FP, Ashburn WL, Conwell RL, et al. CdZnTe solid-state gamma camera. IEEE Trans Nucl Sci 1998;45:359–63.
[25] Hruska CB, O'Connor MK. A Monte Carlo model for energy spectra analysis in dedicated nuclear breast imaging. IEEE Trans Nucl Sci 2008;55:491–500.
[26] Hruska CB, O'Connor MK. CZT detectors: how important is energy resolution for nuclear breast imaging. Phys Medica 2006;21:72–5.
[27] Gruber GJ, Moses WW, Derenzo SE. Monte Carlo simulation of breast tumor imaging properties with compact, discrete gamma cameras. IEEE Trans Nucl Sci 1999;46:2119–23.
[28] Wang B, van Roosmalen J, Piet L, van Schie MA, Beekman FJ, Goorden MG. Voxelized ray-tracing simulation dedicated to multi-pinhole molecular breast tomosynthesis. Biomed Phys Eng Express 2017;3.
[29] Barrett HH, Hunter WCJ, Miller BW, Moore SK, Chen YC, Furenlid LR. Maximum-likelihood methods for processing signals from gamma-ray detectors. IEEE Trans Nucl Sci 2009;56:725–35.
[30] Gray RM, Macovski A. Maximum a posteriori estimation of position in scintillation cameras. IEEE Trans Nucl Sci 1976;23:849–52.
[31] Joung J, Miyaoka RS, Kohlmyer SG, Lewellen TK. Investigation of bias-free positioning estimators for the scintillation cameras. IEEE Trans Nucl Sci 2001;48:715–9.
[32] Hamamatsu. Photomultiplier tubes and related products. Japan: Hamamatsu Photonics K.K.; 2016.
[33] Janecek M, Moses WW. Optical reflectance measurements for commonly used reflectors. IEEE Trans Nucl Sci 2008;55:2432–7.
[34] Jan S, Santin G, Strul D, Staelens S, Assie K, Autret D, et al. GATE: a simulation toolkit for PET and SPECT. Phys Med Biol 2004;49:4543–61.
[35] Jan S, Benoit D, Becheva E, Carlier T, Cassol F, Descourt P, et al. GATE V6: a major enhancement of the GATE simulation platform enabling modelling of CT and radiotherapy. Phys Med Biol 2011;56:881–901.
[36] van der Laan DJ, Schaart DR, Maas MC, Beekman FJ, Bruyndonckx P, van Eijk CWE. Optical simulation of monolithic scintillator detectors using GATE/GEANT4. Phys Med Biol 2010;55:1659–75.
[37] Dorenbos P, deHaas JTM, vanEijk CWE. Non-proportionality in the scintillation response and the energy resolution obtainable with scintillation crystals. IEEE Trans Nucl Sci 1995;42:2190–202.
[38] Moszynski M, Zalipska J, Balcerzyk M, Kapusta M, Mengesha W, Valentine JD. Intrinsic energy resolution of NaI(Tl). Nucl Instrum Meth A 2002;484:259–69.
[39] Moore SK. ModPET: novel applications of scintillation cameras to preclinical PET. The University of Arizona; 2011.
[40] Vinke R, Levin CS. A method to achieve spatial linearity and uniform resolution at the edges of monolithic scintillation crystal detectors. Phys Med Biol 2014;59:2975–95.
[41] NEMA. NEMA Standards Publication NU 1-2007: Performance Measurement of Gamma Cameras. USA: National Electrical Manufacturers Association; 2007.
[42] Villena JL, Tapias G, Lage E, Kreuger R, Beekman FJ. Evaluation of a 25-511keV list mode readout system for a large field-of-view gamma camera. IEEE Nucl Sci Conf R 2010:2168–73.
[43] Hesterman JY, Caucci L, Kupinski MA, Barrett HH, Furenlid LR. Maximum-likelihood estimation with a contracting-grid search algorithm. IEEE Trans Nucl Sci 2010;57:1077–84.
[44] Hunter WCJ. Modeling stochastic processes in gamma-ray imaging detectors and evaluation of a multi-anode PMT scintillation camera for use with maximum-likelihood estimation methods. The University of Arizona; 2007.
[45] Ogawa K, Harata Y, Ichihara T, Kubo A, Hashimoto S. A practical method for position-dependent compton-scatter correction in single photon-emission CT. IEEE Trans Med Imaging 1991;10:408–12.
[46] SensL 2017. http://sensl.com/estore/arrayj-60035-64p-pcb/. [last access: 2017 16 Feb].
[47] Ohara. Optical Glass datasheets. Japan: Ohara Inc.; 2016.